Korean J. Chem. Eng., 40(7), 1623-1632 (2023)
DOI: 10.1007/s11814-023-1427-x

pISSN: 0256-1115
eISSN: 1975-7220

Simulation of the purging process of randomly distributed droplets in a gas diffusion layer using lattice Boltzmann method

Guogang Yang, Jiadong Liao†, Qiuwan Shen†, Shian Li, Ziheng Jiang, Hao Wang, Zheng Li, Guoling Zhang, and Naibao Huang

Marine Engineering College, Dalian Maritime University, Dalian, 116000, China
(*Received 9 September 2022 • Revised 29 December 2022 • Accepted 31 January 2023*)

Abstract−Droplet purging in the gas diffusion layer (GDL) is the key to improving the performance of proton exchange membrane fuel cells (PEMFCs). Lattice Boltzmann method (LBM) is used to study the dynamic behavior of multiple droplets randomly distributed in the GDL under air purging. The GDL is randomly reconstructed. The effects of rib width, initial water content, contact angle and air velocity are studied. By analyzing the dynamic distribution of droplets in the GDL and the change of the remaining water content with time, it is found that the droplets are only a small amount under the rib and accumulated mostly on both sides of the GDL at stabilization, which is caused by the large velocity under the rib. The residual water content in the GDL increases with the increase of the initial water content, and decreases with the increase of the rib width, contact angle and air velocity. However, when the rib to channel width ratio exceeds 1, the improvement of purging effect is not obvious, the purging time increases significantly, and the increase of air velocity does not help much to remove the droplets accumulated on both sides of the GDL.

Keywords: Gas Diffusion Layer, Droplets Random Distribution, Air Purging, Lattice Boltzmann Method, Droplets Dynamic Behavior

INTRODUCTION

The environmental problems caused by the consumption of fossil energy promote the development of the world's energy system towards renewable and environmentally friendly. Proton exchange membrane fuel cells (PEMFCs) have received widespread attention due to their zero emissions, high energy density and low noise [1-3], and have been successfully applied in automobiles, ships, portable devices and other fields [4]. However, the issue of high performance and long life has always been the key to restrict its commercial application [5]. Among them, water management is one of the factors affecting the performance of PEMFCs. If the water content in the fuel cell is too low, the membrane will be dehydrated and the proton conduction will be affected, and conversely, it will cause flooding, affecting hydrogen and oxygen transport [6,7]. The gas diffusion layer (GDL) plays an important role in PEMFC for electron transport, gas transport and generated water discharge. To improve water management in PEMFCs, water transport processes in GDL have been extensively studied.

The experimental research mainly considers the effect of fuel cell operating conditions [8,9] and the design optimization of the fuel cell structure [10], and visualization techniques such as electron microscopy [11], neutron imaging [12], and X-ray radiation [13] can be used to capture the water transport process. However, experimental methods suffer from high cost and low resolution leading to inaccurate measurements, and researchers have developed various numerical models. Xu et al. [14] considered the effects of assembly force, GDL thickness and flow channel structure to study the water motion in GDL under compression by developing a integrated model, and found that the drainage pressure increases with the increase of assembly force, and the 0.2 mm thick GDL and narrower rib are helpful for drainage. Shangguan et al. [15] used the volume of fluid (VOF) method to study the influence of the porosity distribution in the GDL on the transport process of liquid water, and found that the higher the porosity gradient, the smaller the water saturation. Chen et al. [16] coupled finite volume method (FVM) and lattice Boltzmann method (LBM) to simulate fluid flow in GDL, and found that this method can accurately capture pore-scale flow information and save computational resources. Ira et al. [17] investigated the effect of hydrophilic fiber content and compression on water transport in the GDL using LBM and found that appropriate hydrophilic fiber and compression facilitated water drainage. Jeon [18-20] used LBM to study the water transport behavior in two-dimensional GDL, and found that compression, channel rib width and rib structure have a great impact on the water distribution. Kim et al. [21] studied the influence of microporous layer and the surface wettability of multilayer porous transport layers on the water transport behavior in GDL using LBM.

The above studies focus on the process of liquid water flowing from the bottom of the GDL to the flow channel during operation, and mainly analyze the growth of liquid water and its distribution within the GDL after reaching a steady state. Among them, the studies of Jeon and Kim et al. used a reconstruction of the two-dimensional GDL in the form of randomly generated circular solid

†To whom correspondence should be addressed.
E-mail: ljddmu@dlmu.edu.cn, shenqiuwan@dlmu.edu.cn

particles. However, the carbon fibers in the real two-dimensional GDL are not circular particles. Yang et al. [22] showed that the non-uniform pore distribution of the GDL has an important effect on water transport, and the model reflecting the real GDL structure should be used to study water transmission in GDL.

Water management also includes the purging process. After fuel cell shutdown, gas purging is required to remove liquid water from porous electrodes, especially at low temperatures, to prevent liquid water from freezing and expanding in volume to damage the porous media structure [23]. Although the purging process in the GDL is also a gas-liquid two-phase flow problem, the difference is that the gas flows in from the flow channel, and the droplets in the GDL are discharged under the action of the gas. There have been related studies on the process of gas purging droplets in the GDL.

Kakaee et al. [24] studied the influence of polytetraflfluoroethylene (PTFE) distribution and binder content on purging in the GDL and found that the droplet removal is not affected by PTFE distribution when no binder is included, and the addition of binder hinders the droplet removal. Molaeimanesh et al. [25] investigated the influence of the wettability gradient on the discharge of droplets near the rib and near the microporous layer in the GDL, and found that different wettability gradient directions have different effects on the removal of droplets at different positions. They also studied the influence of PTFE distribution on droplet removal within the GDL and found that carbon fibers not treated with PTFE hinder droplet removal [26]. In addition, they also found that there are two mechanisms of droplet removal within the GDL, inertial jetting and evaporation, which are affected by the GDL contact angle and initial droplet size [27]. They then investigated the influence of compression of GDL on droplet discharge and found that proper compression can speed up droplet removal, but greater compression will prevent droplet removal [28]. Niu et al. [29] studied the flow of droplets at different locations under air purging and found that the droplet located at the corner of flow channel is more likely to pass through the GDL when the flow channel pressure is higher. Chen et al. [30] studied the influence of rib width and GDL contact angle on purging the droplet and found that the larger the contact angle and the narrower the rib, the smaller the residual saturation in the GDL.

From the above literature, it can be seen that the current studies mainly consider the effects of wettability (including PTFE distribution and gradient variation), droplet position, compression, rib width, and binder content on the droplet purging effect in the GDL, and they all focus on individual droplet flow. For the study of wettability gradient, because a single droplet cannot experience the whole process of wettability change, the research method is inappropriate. The results of ex situ experiments by Nam and Kaviany [31] show that liquid water vapor randomly condenses into small droplets or thin films in the GDL. In situ experiment by Turhan et al. [32] using neutron images also observes that in an operating PEMFC, this distribution of droplet separation is present for a short period of time after cell start-up. This physical model for the random distribution of droplets of different sizes in the GDL is used in the studies of Chen et al. [33] and Mukherjee et al. [34] In a recent study, Wang et al. [35] investigated the effect of randomly distributed droplets within a GDL on mass transport. The experimental observations as well as the physical structure used in the researchers' numerical simulations indicate that random distribution of droplets within the GDL exists and is of research significance. Therefore, the research object of this paper is multiple droplets with different radii randomly distributed in the GDL.

LBM is a mesoscopic simulation method without the limitation of continuous medium assumption compared to traditional computational fluid dynamics (CFD) methods, which gives the method better accuracy in simulating microchannel flows. It is very suitable for dealing with porous media flow problems due to its unique advantages in complex boundary treatment. In recent years LBM has been widely used to study gas flow at the micro- and nano-scale [36-38], multiphase flows in porous media [39-41], etc.

In this paper, a random reconstruction method is used to generate a GDL model reflecting the real structure, and multiple droplets of different sizes are randomly distributed in the GDL, and the droplet transport process under air purging is simulated based on a single relaxation time multi-component multiphase LB model to investigate the effects of different rib widths, water contents, contact angles and air velocities on the droplet motion in the GDL. The dynamic distribution of droplets in the GDL and the variation of the remaining water content with time are analyzed in detail. It provides a theoretical reference for understanding the dynamic behavior of multiple droplets in GDL in line with the actual situation during purging.

NUMERICAL METHODS

1. Multicomponent Multiphase LB Model

At present, many LB multicomponent multiphase flow models have been proposed and applied. The common ones are the color model [42], the pseudopotential model [43] and the free energy model [44]. The above models have their own advantages and disadvantages. Among them, the pseudopotential model has received extensive attention due to its features such as automatic tracking of the phase interface, high computational efficiency, easy programming, and easy handling of wall wettability. In this paper, the Shan and Chen (SC) pseudopotential multicomponent model with interparticle force is used as the research model to simulate the multiphase flow process in the GDL, and the velocity format is D2Q9. The evolution of the distribution function is as follows:

$$f_i^{\sigma}(x + c_i\delta_t, t + \delta_t) = f_i^{\sigma}(x, t) - \frac{1}{\tau^{\sigma}}[f_i^{\sigma}(x, t) - f_i^{\sigma, eq}(x, t)] \quad (1)$$

where the superscript σ represents the fluid component; i is the direction of the discrete velocity, i=1, 2, 3, ...9; $f_i^{\sigma}(x, t)$ refers to the distribution function of the σ particle at the x position at time t; $f_i^{\sigma}(x+c_i\delta_t, t+\delta_t)$ is the distribution function of the σ particle at the x adjacent position $x+c_i\delta_t$ after a time step δ_t; the density ρ and velocity u of each component are obtained by the distribution function.

$$\rho_{\sigma} = \sum_i f_i^{\sigma} \quad (2)$$

$$u_{\sigma} = \sum_i c_i f_i^{\sigma} / \rho_{\sigma} \quad (3)$$

c_i is the discrete velocity, defined as follows:

$$c_i=\begin{cases}\left(\cos\left[\frac{(i-1)\pi}{2}\right],\ \sin\left[\frac{(i-1)\pi}{2}\right]\right) & i=1,\ 2,\ 3,\ 4\\ \left(\sqrt{2}\cos\left[\frac{(i-5)\pi}{2}+\frac{\pi}{4}\right],\ \sqrt{2}\sin\left[\frac{(i-5)\pi}{2}+\frac{\pi}{4}\right]\right) & i=5,\ 6,\ 7,\ 8\\ (0,\ 0) & i=9\end{cases} \tag{4}$$

τ^{σ} is the relaxation time of the σ particle, $\upsilon^{\sigma}=c_s^2(\tau^{\sigma}-0.5)$, c_s is the lattice sound velocity, $c_s^2=1/3$. $f_i^{\sigma,eq}(x,\ t)$ is the equilibrium state distribution function of the σ particle, and the expression is:

$$f_i^{\sigma,\,eq}=\omega_i\rho_{\sigma}\left[1+\frac{c_i\cdot u_{\sigma}^{eq}}{c_s^2}+\frac{(c_i\cdot u_{\sigma}^{eq})^2}{2c_s^4}-\frac{u_{\sigma}^{eq^2}}{2c_s^2}\right] \tag{5}$$

where ω_i is the weighting factor, $\omega_{1,\,2,\,3,\,4}=1/9$, $\omega_{5,\,6,\,7,\,8}=1/36$, $\omega_9=4/9$. u_{σ}^{eq} is the equilibrium velocity of the σ particle, which is also the macroscopic velocity, and the expression is given in Eq. (6).

$$u_{\sigma}^{eq}=\frac{\sum_{\sigma}\rho_{\sigma}u_{\sigma}/\tau_{\sigma}}{\sum_{\sigma}\rho_{\sigma}/\tau_{\sigma}}+\frac{\tau_{\sigma}F_{\sigma}}{\rho_{\sigma}} \tag{6}$$

where F_{σ} is the resultant force on the σ particle, $F_{\sigma,\,coh}$ is the fluid-fluid interaction force, and $F_{\sigma,\,adh}$ is the fluid-solid interaction force.

$$F_{\sigma,\,coh}=-\psi_{\sigma}(x)\sum_i G_{\sigma\bar{\sigma}}(x+c_i\delta t)\psi_{\bar{\sigma}}(x+c_i\delta t)c_i \tag{7}$$

$$G_{\sigma\bar{\sigma}}(x+c_i\delta t)=\begin{cases}4g & i=1,\ 2,\ 3,\ 4\\ g & i=5,\ 6,\ 7,\ 8\\ 0 & i=9\end{cases} \tag{8}$$

$$F_{\sigma,\,adh}=-\psi_{\sigma}(x)\sum_i W(x+c_i\delta t)s(x+c_i\delta t)c_i \tag{9}$$

$$W(x+c_i\delta t)=\begin{cases}4w & i=1,\ 2,\ 3,\ 4\\ w & i=5,\ 6,\ 7,\ 8\\ 0 & i=9\end{cases} \tag{10}$$

where ψ_{σ} is the potential function of the σ particle, $\psi_{\sigma}=1-\exp(-\rho_{\sigma})$. The subscripts σ and $\bar{\sigma}$ indicate different components, g is the strength coefficient of the fluid-fluid interaction force, and w is the strength coefficient of the fluid-solid interaction force. s is the switching function, which is equal to 1 at the solid point and 0 at the fluid point.

2. Model Validation

(1) Droplet test

The droplet test is used to verify whether the above multi-component multiphase SC model conforms to Laplace's law. The expression of Laplace's law is given by Eq. (11).

$$\Delta P=\frac{\lambda}{R} \tag{11}$$

$$P=c_s^2\sum_{\sigma}\rho_{\sigma}+\frac{c_s^2}{2}\sum_{\sigma,\,\bar{\sigma}}G_{\sigma\bar{\sigma}}\psi_{\sigma}\psi_{\bar{\sigma}} \tag{12}$$

where P is the pressure, ΔP is the difference between the internal and external pressures of the droplet, λ is the surface tension, and R is the radius of the droplet.

The specific implementation process is as follows: droplets of different radii are placed in a square computational domain with a lattice number of 100×100. The four boundaries of the computational domain are all periodic boundaries, and the droplets gradually tend to be stable under the flow-flow interaction force, and the droplet radius and pressure difference at the time of stabilization are recorded. The initial density is set to 2 for water and 10^{-5} for air inside the droplet, and 10^{-5} for water and 2 for air outside the droplet, and this density setting is also applied in Refs. [45,46]. According to the previous work [47], the fluid-fluid interaction force strength coefficient takes the value g=0.09. Fig. 1(a) shows the simulation results, and it can be seen that 1/R has a linear relationship with ΔP, and the slope is the surface tension, which is 0.239. It is shown that the LB model satisfies Laplace's law.

(2) Static contact angle test

The wettability of the wall is usually characterized by the static contact angle. The wettability of the wall is changed by setting the strength coefficient of the solid-liquid interaction force w. In a square

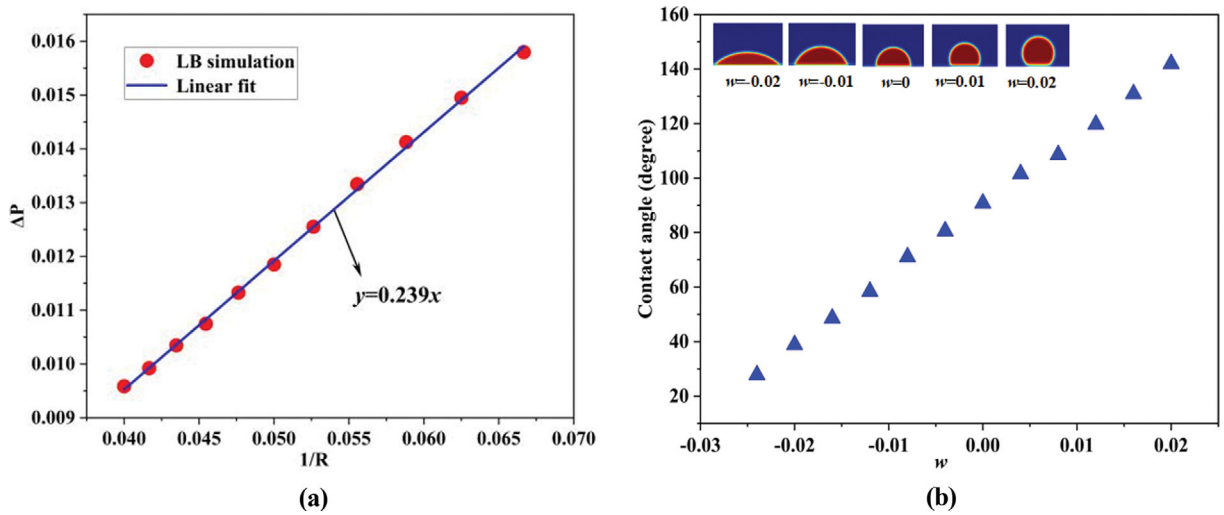

Fig. 1. Model verification: (a) the relationship between the reciprocal of the droplet radius and the pressure difference, (b) the relationship between the fluid-solid interaction force strength coefficient w and the contact angle.

computational domain with a lattice number of 100×100, the bounce boundary is applied to the upper and lower boundaries, and the periodic boundary is applied to the left and right boundaries. The droplet is placed on the lower wall, and after stabilization, the contact angle is calculated using Eq. (13), (14) [48].

$$R=\frac{4H^2+L^2}{8H} \tag{13}$$

$$\theta=\begin{cases}180-\arctan\left(\frac{L}{2(H-R)}\right), & (H>R)\\ \arctan\left(\frac{L}{2(R-H)}\right), & (H\le R)\end{cases} \tag{14}$$

where R is the radius of the droplet, θ is the contact angle between the droplet and the wall, H is the height of the droplet, and L is the length of the contact line between the droplet and the wall. The relationship between w and θ is given in Fig. 1(b). The simulation results show that different w values have corresponding contact angles. In this paper, the w values corresponding to 100°, 120°, and 140° required for the simulation are 0.004, 0.012, and 0.02, respectively.

3. Computational Domain and Boundary Conditions

The interdigitated flow field is widely used in fuel cells due to its efficient flow field design [49], its structure is shown in Fig. 2(a). The two-dimensional (2D) computational domain of this paper is shown in Fig. 2(b). The 2D GDL is a section taken from the reconstructed three-dimensional (3D) GDL. The 3D GDL reconstruction has been done in previous work [50]. Researchers have different choices about GDL dimesion, as shown in Table 1. It can be seen that the dimesion of 2,000×200 μm^2 is chosen more often, and in addition, the larger the dimesion is, the more computational resources are required. Therefore, the GDL dimesion of 2,000×200 μm^2 and the rib width of 1,000 μm^2 are chosen in this paper under the premise of satisfying the dimensional rationality and saving computational resources. Other parameters of GDL are the same as those of Chen et al. [30]. To verify the validity of the reconstructed 2D GDL structure, the permeability in the in-plane direction and through-plane direction are simulated and calculated, and the results are 3.58×10^{-11} m^2 and 2.12×10^{-11} m^2, respectively. The experimentally measured permeability of Tory 090 GDL (0.80 porosity) by Gostick et al. [51] is 8.99×10^{-12} m^2 in the in-plane direction and 2×10^{-11} m^2 in the through-plane direction. The large result is mainly due to the large porosity (0.87), and the result is reasonable and acceptable.

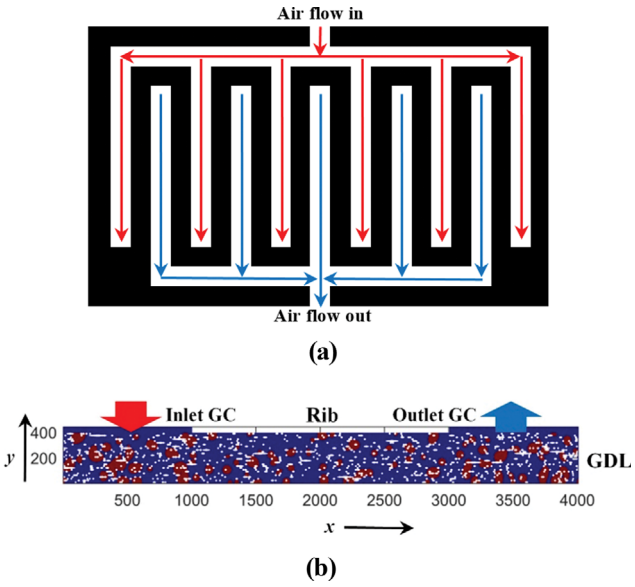

Fig. 2. Interdigitated flow field of PEMFC: (a) top view, (b) computational domain.

Table 1. GDL dimesion in literature

Literature sources	GDL dimesion/μm^2	Rib width/μm
Yang et al. [22]	2,400×250	1,200
Molaeimanesh et al. [25]	2,000×200	1,000
Chen et al. [30]	2,000×200	1,000
Wang et al. [35]	2,000×200	1,000
Ding et al. [52]	2,200×215	1,300
Shi et al. [53]	2,000×250	1,000

To verify the grid independence, the computational domains with grid numbers of 2,000×200, 3,400×340, 4,000×400, and 5,000×500 are simulated respectively, and it is found that the computational domain with grid number of 4,000×400 meets the requirements. At this time, 1 lattice represents 0.5 μm, and the length unit conversion coefficient C_l is 0.5×m.

As shown in Fig. 2(b), blue represents air, red represents droplets, and white represents carbon fibers and rib. The size and position of the droplets in the GDL are randomly distributed at the initial moment. After the droplets form a stable contact angle on the solid wall, air is introduced into the flow channel inlet for purging, and the air velocity is 1.5 m/s [30]. Keeping the Reynolds number at the air inlet constant, the physical unit is converted into a lattice unit (lu), the corresponding velocity is 0.008 lu, and the velocity unit conversion coefficient C_v is 187.5 m/s. A time step representing the physical time can be calculated as 2.67×10^{-9} s based on C_l and C_v. The Zouhe velocity and pressure boundaries [54] are used for the inlet and outlet of the channel respectively, the left and right boundaries of the computational domain are symmetrical boundaries, and the bottom of the GDL, carbon fibers and rib are set as standard rebound boundaries.

RESULTS AND DISCUSSION

1. Effect of Different Rib Widths

This paper characterizes the rib width in terms of the width ratio of the rib to the channel. The variation of droplet distribution in the GDL from initial to steady state under air purging for different rib widths is given in Fig. 3. The water distribution and water content are the same at the initial moment. It can be seen that the droplets preferentially choose large pores to flow out of the GDL. In addition, the droplets flow under the ribs obviously, and the droplets in the small pores are extremely difficult to be purged, and they are mostly concentrated at the bottom of the GDL. Droplets are easy to accumulate near both sides of the GDL, which is

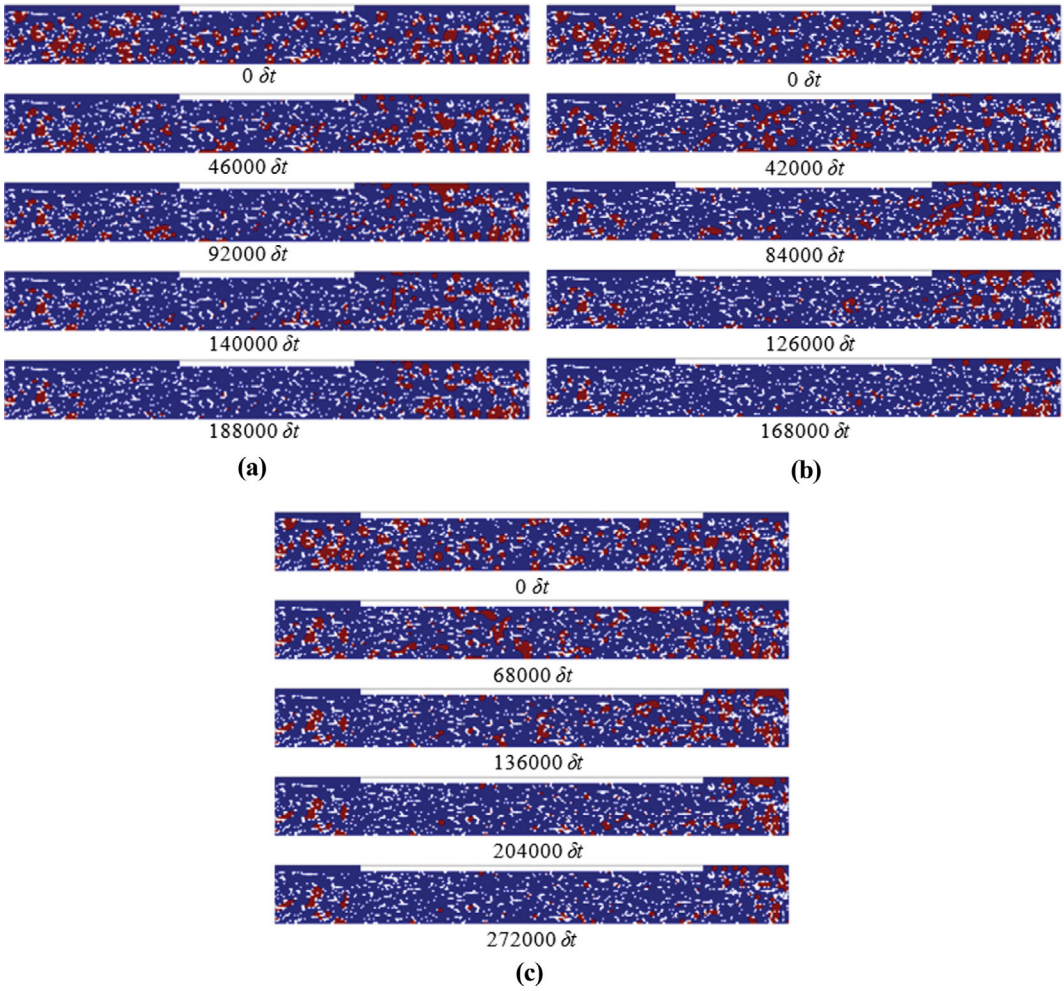

Fig. 3. The distribution of droplets in GDL varies with time under different rib-channel width ratios: (a) 1 : 2, (b) 1 : 1, (c) 2 : 1.

difficult to purge, and the droplets accumulated on the outlet side are significantly more than those on the inlet side. The narrower the rib, the more droplets accumulated on both sides of the GDL. To explain this phenomenon, the pressure distribution and velocity vector diagram within the GDL at stabilization is given in Fig. 4. It is obvious that the closer to the air inlet, the higher the pressure, and the wider the rib, the lower the pressure at the inlet, and the more uniform the pressure distribution of the entire GDL, indicating that the less the droplets block the pores. The velocity under the rib is relatively large, and the closer to the rib, the larger the velocity, and the velocity at the exit side near the rib is the largest. The velocity on both sides of the GDL is almost 0, and it is difficult for the air to purge, so the droplets on both sides are difficult to discharge. For the outlet side to accumulate more droplets than the inlet side, this is because under the air purging, the droplets flow to the outlet side and accumulate in the area where the air is difficult to purge, while the droplets on the inlet side are mainly the residues of the initial state, and there is no accumulation of other droplets.

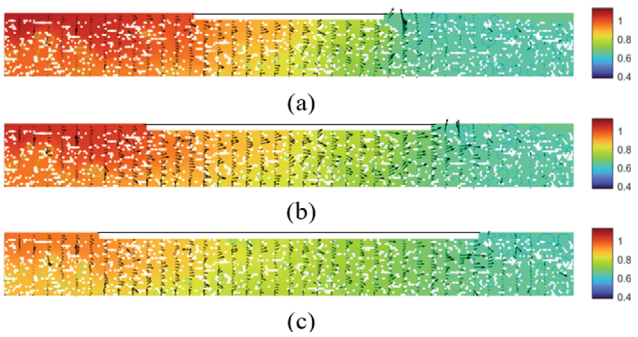

Fig. 4. The pressure distribution and velocity vector diagram in the GDL: (a) 1 : 2, (b) 1 : 1, (c) 2 : 1.

The curves of the remaining water content in the GDL with time for different rib widths are given in Fig. 5. It can be seen that before 120,000 time steps (0.32 ms), the narrower the rib, the greater the water discharge rate. This is due to the higher inlet pressure. With the increase of time, the droplets in the large pores under the ribs are exhausted, and the accumulation of droplets on both sides is difficult to be purged. The earliest to reach stability is the case of rib-channel width ratio of 1 : 1, the time is 168,000 time steps (0.45 ms). The wider the rib, the lowest water content in the GDL when stable. The case of rib-channel width ratio of 2 : 1 has the lowest final water content of 6.73%, but it is only 0.51% less than the case

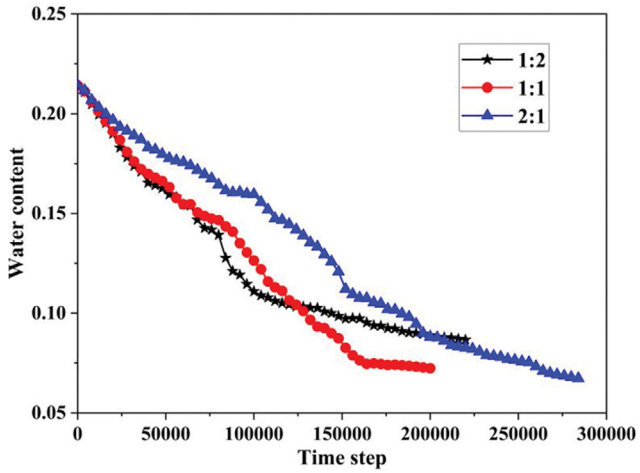

Fig. 5. Change of residual water content in GDL with time.

of channel width ratio of 1 : 1, and the time to reach stability is the longest, 272,000 time steps (0.73 ms), which is 61.90% longer than the case of the rib-channel width ratio of 1 : 1. This conclusion differs from Chen et al. [30], mainly because it only considers the purging of a single droplet in the middle of the GDL, and there is no droplet accumulation on both sides, so the shorter the rib, the faster the droplet is discharged and the lower the remaining water content.

2. Effect of Different Water Contents

Fig. 6(a)-(c) show the movement process of droplets in the GDL with initial water content of 10%, 22%, and 30% under air purging, respectively. The comparison shows that the more the initial water content in the GDL, the more the droplets inside the small pores under the rib that are not purged. This is because the more the initial water content in the GDL, the greater the probability of droplets occupying the small pores or entering the small pores during the purging process, and the shear force of the air on the droplets is smaller than the capillary force on the droplets, the droplets in the small pores are difficult to be discharged. The more the initial water content in GDL, the more the droplets accumulate at the outlet side during the purging process. Due to the presence of a region on the outlet side where air is difficult to purge, the droplets in this region will not be discharged.

Fig. 6(d) shows the variation of residual water content with time during the purging process in GDL with different initial water content. It can be seen that the smaller the initial water content, the sooner the stability is reached, the smaller the remaining water

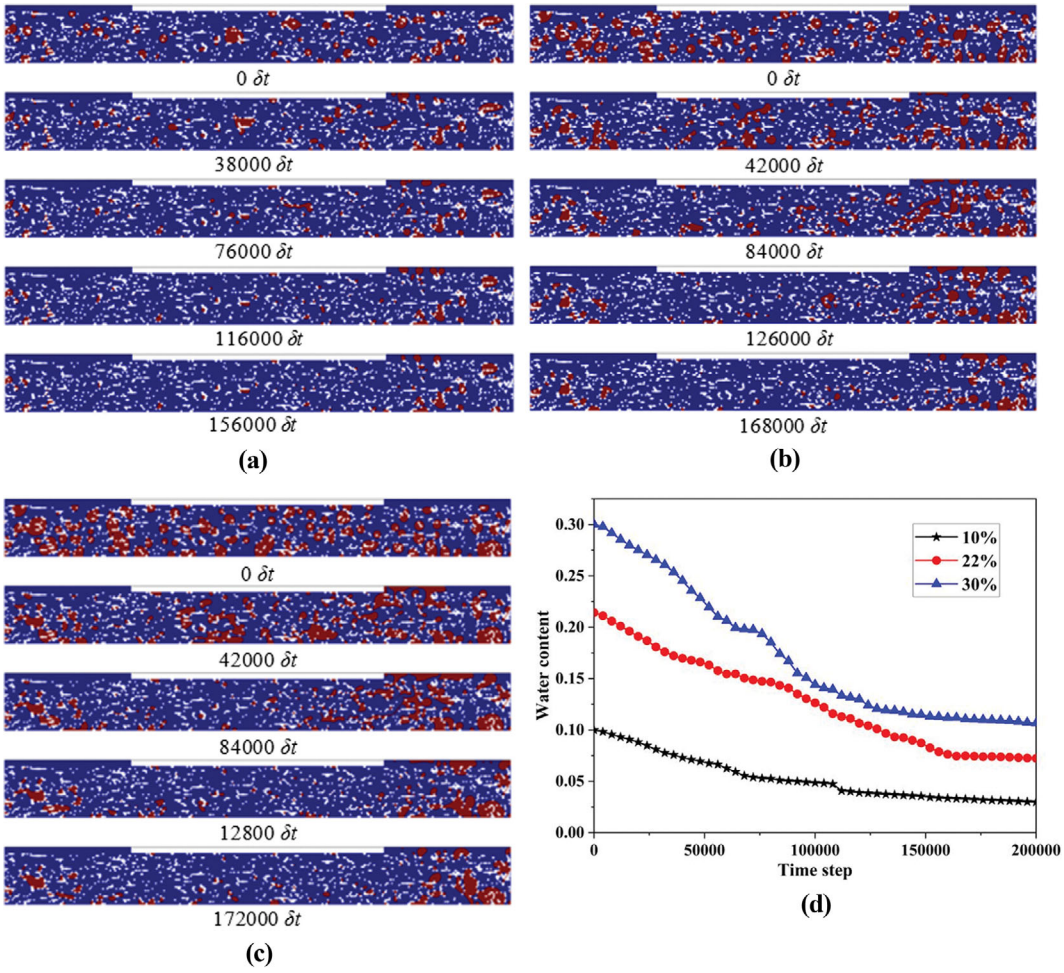

Fig. 6. The variation of droplets distribution and water content with time in GDL: (a) 10%, (b) 22%, (c) 30%, (d) water content.

content, and the smaller the amount of water discharged from the GDL. The initial water content of 10%, 22% and 30% reaches the stability time of 156,000 δt (0.42 ms), 168,000 δt (0.45 ms) and 172,000 δt (0.46 ms) respectively, the remaining water content is 2.98%, 7.24% and 10.65% respectively, and the water volume swept out of GDL is 7.12%, 14.76% and 19.35% respectively. Owejan et al. [55] investigated the water content variation within the GDL during purging by an experimental method combining ex situ and in situ methods with neutron imaging diagnostics and found that the higher the water saturation, the higher the remaining water content after purging and the longer the purging time. This result is the same as the simulation result of this paper. In addition, the same conclusion was obtained by the numerical simulation method by Cho et al. [56] and Xu et al. [57]. The main reason is that the more water content, the more droplets accumulated on both sides, and the more droplets in the large pores that can be purged, resulting in longer purge time.

3. Effect of Different Contact Angles

Fig. 7(a)-(c) show the movement process of droplets under air purging at GDL contact angles of 100°, 120°, and 140°, respectively. The initial liquid water content within the GDL is the same. As the purge proceeds, the droplets flow toward the outlet. The droplets that are not purged in the small pores under the rib decrease with increasing contact angle. This is because the larger the GDL contact angle, the greater the capillary force of the pores on the droplets, and the more difficult it is for the droplets to enter the small pores. In addition, the larger the contact angle, the less droplets accumulated on both sides of the GDL at stabilization. The main reason is that the larger the contact angle, the smaller the fluid-solid force on the droplet. It can be seen from Fig. 4 that there is still a small flow velocity on both sides of the GDL, so some droplets can be discharged under a small air shear force.

Fig. 7(d) shows the variation of residual water content with time during the purging process of GDL with different contact angles. It is obvious that the larger the contact angle, the longer the stabilization time and the smaller the residual water content. The GDL with a contact angle of 140° has the longest time to reach stability under air purging, which is 176,000 time steps (0.47 ms), and the smallest residual water content, which is 5.84%. This is because the larger the contact angle, the smaller the viscous force of the fiber to the droplet, the easier the droplet is to be discharged, and the greater the amount of drainage, resulting in a longer purge time.

4. Effect of Different Air Velocities

Fig. 8(a)-(c) show the movement process of the droplets with

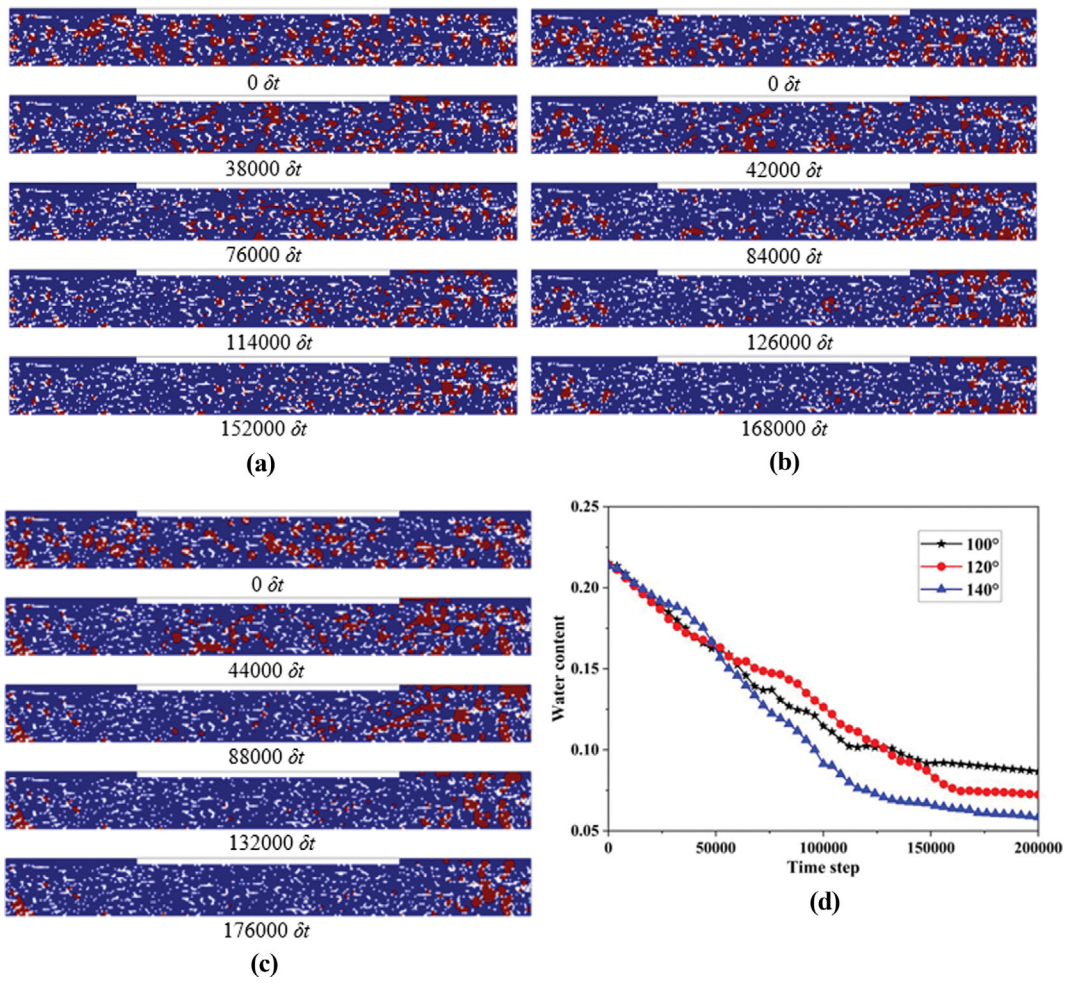

Fig. 7. The variation of droplets distribution and water content with time in GDL: (a) 100°, (b) 120°, (c) 140°, (d) water content.

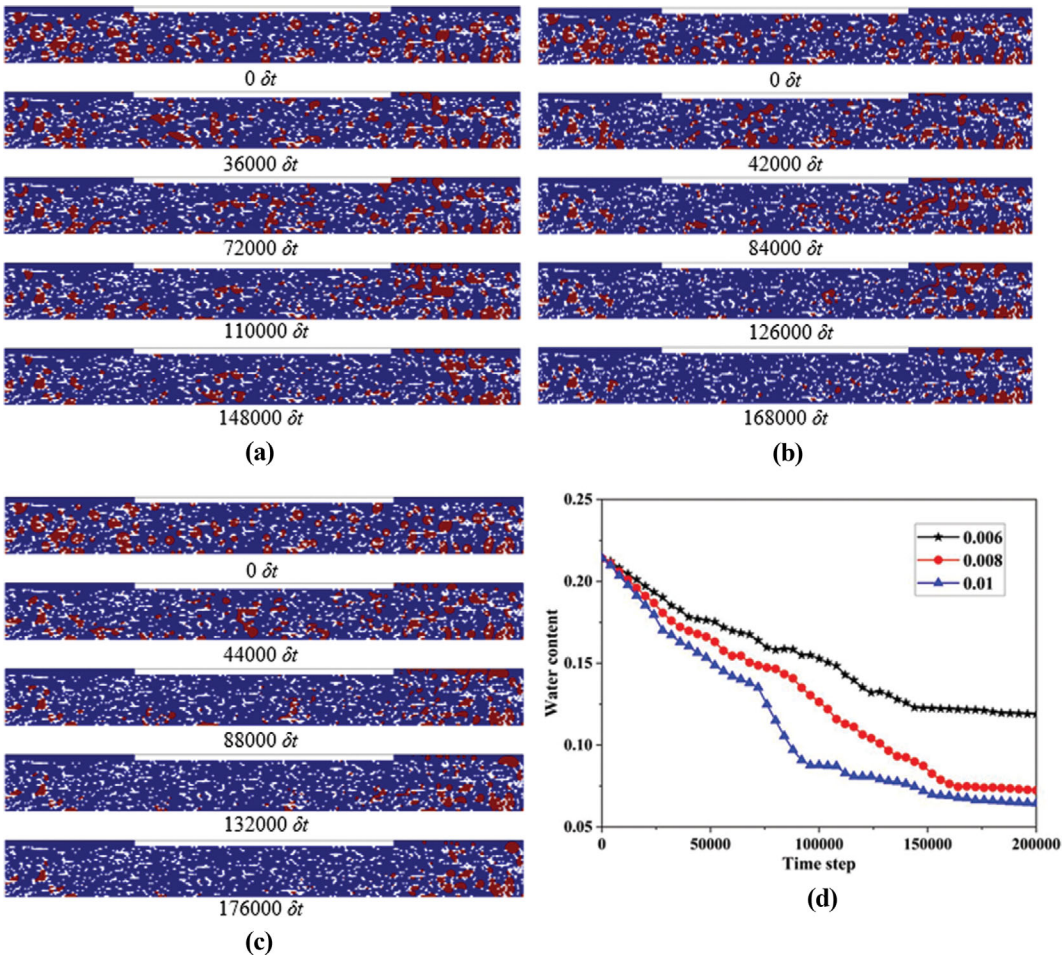

Fig. 8. The variation of droplets distribution and water content with time in GDL: (a) 0.006, (b) 0.008, (c) 0.01, (d) water content.

the same initial distribution in the GDL under the air purging with flow velocities of 0.006, 0.008, and 0.01, respectively. It can be seen that when the air flow velocity is 0.006, the droplets in the GDL are difficult to be purged, and there are a large number of droplets under the rib and on both sides of the GDL when stable. With the increase of the air flow velocity, the droplets remaining under the rib are significantly reduced. Although there are still many droplets accumulated on both sides of the GDL, it is significantly reduced compared with the case where the flow velocity is 0.006. This is because the greater the air velocity, the greater the shear force on the droplets, which is sufficient to overcome the capillary force of the small holes on the droplets, making the droplets easy to be purged.

Fig. 8(d) shows the curve of the remaining water content in the GDL with time during the purging process for different air flow velocities. It can be seen that the larger the air flow velocity, the faster the droplet flow, the smaller the remaining water content in the GDL, and the longer the time to reach stability. The air flow velocities of 0.006, 0.008, and 0.01 corresponded to 11.89%, 7.24%, and 6.44% of the remaining water content in the GDL, respectively, and the time to reach stability is 148,000 δt, 168,000 δt, and 176,000 δt, respectively. In addition, increasing the air flow velocity from 0.006 to 0.008 increases the drainage rate ((initial water content - remaining water content)/initial water content) by 21.17%, but increasing the air flow velocity from 0.008 to 0.01 increases the drainage rate by only 3.60%, indicating that increasing the air flow velocity does not help much in removing the droplets accumulated on both sides of the GDL.

CONCLUSIONS

Based on the pseudopotential multi-component SC model, the dynamic process of the droplet being purged in the GDL is simulated. By analyzing the effects of rib width, initial water content, contact angle and air flow velocity, the following conclusions are drawn.

(1) Droplets below the rib are easily purged, droplets on both sides of the GDL tend to accumulate, and most of the remaining water content at stabilization is on both sides of the GDL. This is mainly because the velocity below the rib is large and the velocity on both sides of the GDL is particularly small.

(2) The larger the rib width, the lowest water content in the GDL at stabilization. However, the rib-channel width ratio of 2 : 1 is only 0.51% less than that of 1 : 1, and the time to reach stability is 61.90% higher. Therefore, the wider the rib is not better, and the actual need to be determined according to the water removal effi-

ciency.

(3) The larger the initial water content, the larger the water content in the GDL at stabilization, and the longer the purging time. The residual water content in the GDL decreased with the increase of the contact angle and air velocity. However, the increase in air velocity does not improve the purging effect significantly, and the drainage rate only increases by 3.60% when the air velocity increases from 0.008 to 0.01, indicating that increasing the air velocity does not help much in removing the droplets accumulated on both sides of the GDL.

ACKNOWLEDGEMENTS

This work is supported by the National Natural Science Foundation of China (No. 51779025), Natural Science Foundation of Liaoning Province (No. 2020-HYLH-38), and Science and Technology Innovation Foundation of Dalian, China (2021JJ11CG004).

DECLARATION OF COMPETING INTEREST

The authors declare that they have no known competing financial interests or personal relationships that could have appeared to influence the work reported in this paper.

REFERENCES

1. J. D. Liao, G. G. Yang, S. A. Li, Q. W. Shen, Z. H. Jiang, H. Wang and Z. Li, *J. Power Sources*, **529**, 231245 (2022).
2. H. Wang, G. G. Yang, S. A. Li, Q. W. Shen, J. D. Liao, Z. H. Jiang, M. Espinoza-Andaluz, F. M. Su and X. X. Pan, *Int. J. Hydrogen Energy*, **46**(42), 22107 (2021).
3. Z. H. Jiang, G. G. Yang, S. A. Li, Q. W. Shen, J. D. Liao, H. Wang, M. Espinoza-Andaluz, R. M. Ying and X. X. Pan, *Comput. Mater. Sci.*, **190**, 110286 (2021).
4. T. Wilberforce, A. Alaswad, A. Palumbo, M. Dassisti and A. G. Olabi, *Int. J. Hydrogen Energy*, **41**(37), 16509 (2016).
5. T. Wilberforce, Z. El-Hassan, F. N. Khatib, A. Al Makky, A. Baroutaji, J. G. Carton and A. G. Olabi, *Int. J. Hydrogen Energy*, **42**(40), 25695 (2017).
6. K. Jiao and X. Li, *Prog. Energy Combust. Sci.*, **37**(3), 221 (2011).
7. O. S. Ijaodola, Z. El-Hassan, E. Ogungbemi, F. N. Khatib, T. Wilberforce, J. Thompson and A. G. Olabi, *Energy*, **179**, 246 (2019).
8. Q. Yan, H. Toghiani and H. Causey, *J. Power Sources*, **161**(1), 492 (2006).
9. Q. Zhang, R. Lin, L. Técher and X. Cui, *Energy*, **115**, 550 (2016).
10. B. Laoun, H. A. Kasat, R. Ahmad and A. M. Kannan, *Energy*, **151**, 689 (2018).
11. X. Xie, G. Zhang, J. Zhou and K. Jiao, *Int. J. Hydrogen Energy*, **42**(17), 12521 (2017).
12. J. I. S. Cho, T. P. Neville, P. Trogadas, Q. Meyer, Y. Wu, R. Ziesche, P. Boillat, M. Cochet, V. Manzi-Orezzoli, P. Shearing, D. J. L. Brett and M. O. Coppens, *Energy*, **170**, 14 (2019).
13. J. Lee, J. Hinebaugh and A. Bazylak, *J. Power Sources*, **227**, 123 (2013).
14. Y. F. Xu, D. K. Qiu, P. Y. Yi, S. H. Lan and L. F. Peng, *Int. J. Hydrogen Energy*, **44**(26), 13777 (2019).
15. X. Shangguan, Y. Li, Y. Z. Qin, S. B. Cao, J. F. Zhang and Y. Yin, *Electrochim. Acta*, **371**, 137814 (2021).
16. L. Chen, H. B. Luan, Y. L. Feng, C. X. Song, Y. L. He and W. Q. Tao, *Int. J. Heat Mass Tran.*, **55**, 3834 (2012).
17. Y. Ira, Y. Bakhshan and J. Khorshidimalahmadi, *Int. J. Hydrogen Energy*, **46**(33), 17397 (2021).
18. D. H. Jeon and H. Kim, *J. Power Sources*, **294**, 393 (2015).
19. D. H. Jeon, *J. Power Sources*, **423**, 280 (2019).
20. D. H. Jeon, *J. Energy Inst.*, **92**(3), 755 (2019).
21. K. N. Kim, J. H. Kang, S. G. Lee, J. H. Nam and C. J. Kim, *J. Power Sources*, **278**, 703 (2015).
22. M. Yang, A. Du, J. Liu and S. Xu, *World Electric Vehicle J.*, **12**(3), 133 (2021).
23. P. Xu and S. C. Xu, *Fuel Cells*, **17**(6), 794 (2017).
24. A. H. Kakaee, G. R. Molaeimanesh and M. E. Garmaroudi, *Int. J. Hydrogen Energy*, **43**(32), 15481 (2018).
25. G. R. Molaeimanesh and M. H. Akbari, *Korean J. Chem. Eng.*, **31**(4), 598 (2014).
26. G. R. Molaeimanesh and M. H. Akbari, *Int. J. Hydrogen Energy*, **39**(16), 8401 (2014).
27. G. R. Molaeimanesh and M. H. Akbari, *Int. J. Hydrogen Energy*, **41**(33), 14872 (2016).
28. G. R. Molaeimanesh, M. H. Shojaeefard and M. R. Moqaddari, *Korean J. Chem. Eng.*, **36**(1), 136 (2019).
29. Z. Q. Niu, K. Jiao, Y. Wang, Q. Du and Y. Yin, *Int. J. Energy Res.*, **42**(2), 802 (2018).
30. L. Chen, H. B. Luan, Y. L. He and W. Q. Tao, *Int. J. Therm. Sci.*, **51**, 132 (2012).
31. J. H. Nam and M. Kaviany, *Int. J. Heat Mass Transf.*, **46**, 4595 (2003).
32. A. Turhan, S. Kim, M. Hatzell and M. M. Mench, *Electrochim. Acta*, **55**, 2734 (2009).
33. L. Chen, H. B. Luan, Y. L. He and W. Q. Tao, *Russ. J. Electrochem.*, **48**(7), 712 (2012).
34. P. P. Mukherjee, C. Y. Wang and Q. Kang, *Electrochim. Acta*, **54**(27), 6861 (2009).
35. H. Wang, G. Yang, S. Li, Q. Shen, F. Su, Z. Jiang, J. Liao and X. Pan, *Energy Fuels*, **36**(15), 8422 (2022).
36. Z. H. Chai, Z. L. Guo, L. Zheng and B. C. Shi, *J. Appl. Phys.*, **104**(1), 014902 (2008).
37. C. Gao, R. N. Xu and P. X. Jiang, *Int. J. Numer. Methods Heat Fluid Flow*, **25**(8), 1957 (2015).
38. C. M. Freeman, G. J. Moridis and T. A. Blasingame, *Transp. Porous Media*, **90**(1), 253 (2011).
39. H. B. Huang, L. Wang and X. Y. Lu, *Comput. Math. Appl.*, **61**(12), 3606 (2011).
40. H. B. Huang, Z. T. Li, S. S. Liu and X. Y. Lu, *Int. J. Numer. Methods Fluids*, **61**(3), 341 (2009).
41. Q. Li, K. H. Luo, Q. J. Kang, Y. L. He, Q. Chen and Q. Liu, *Prog. Energy Combust. Sci.*, **52**, 62 (2016).
42. A. K. Gunstensen, D. H. Rothman, S. Zaleski and G. Zanetti, *Phys. Rev. A*, **43**(8), 4320 (1991).
43. X. Shan and H. Chen, *Phys. Rev. E*, **47**(3), 1815 (1993).
44. M. R. Swift, W. R. Osborn and J. M. Yeomans, *Phys. Rev. Lett.*, **75**(5), 830 (1995).
45. J. Park and X. Li, *J. Power Sources*, **178**, 248 (2008).
46. L. Chen, H. B. Luan and W. Q. Tao, *Front. Heat Mass Transf.*, **1**(2)

023002 (2010).
47. J. D. Liao, G. G. Yang, Q. W. Shen, S. A. Li, Z. H. Jiang, H. Wang, Z. H. Sheng, G. L. Zhang and H. P. Zhang, *Energy Fuels*, **35**(20), 16799 (2021).
48. H. B Huang, M. Sukop and X. Y. Lu, *Multiphase lattice Boltzmann methods: Theory and application*, Wiley, New York, 79 (2015).
49. T. V. Nguyen, *J. Electrochem. Soc.*, **143**(5), 103 (1996).
50. J. D. Liao, G. G. Yang, S. A. Li, Q. W. Shen, Z. H. Jiang, H. Wang, L. Y. Xu, M. Espinoza-Andaluz and X. X. Pan, *Energy Fuels*, **35**(3), 2654 (2021).
51. J. T. Gostick, M. W. Fowler, M. D. Pritzker, M. A. Ioannidis and L. M. Behra, *J. Power Sources*, **162**, 228 (2006).
52. J. Ding, Y. T. Mu, S. Zhai and W. Q. Tao, *Int. J. Heat Mass Transf.*, **103**, 744 (2016).
53. Z. Shi, X. Wang and L. Guessous, *J. Fuel Cell Sci. Technol.*, **7**(2), 021012 (2010).
54. Q. S. Zou and X. Y. He, *Phys. Fluids*, **9**, 1591 (1997).
55. J. P. Owejan, J. J. Gagliardo, S. R. Falta and T. A. Trabold, *J. Electrochem. Soc.*, **156**(12), B1475 (2009).
56. K. T. Cho and M. M. Mench, *Int. J. Hydrog. Energy*, **35**(22), 12329 (2010).
57. P. Xu and S. Xu, *Fuel Cells*, **17**(6), 794 (2017).